J. Fluid Mech. (1994), *vol.* 272, *pp.* 255–284

Three-dimensional wave instability near a critical level

By K. B. WINTERS[1] AND E. A. D'ASARO[2]

[1] Department of Applied Mathematics and Applied Physics Laboratory, University of Washington, Seattle, WA 98105, USA

[2] Department of Oceanography and Applied Physics Laboratory, University of Washington, Seattle, WA 98105, USA

(Received 27 March 1992 and in revised form 11 February 1994)

The behaviour of internal gravity wave packets approaching a critical level is investigated through numerical simulation. Initial-value problems are formulated for both small- and large-amplitude wave packets. Wave propagation and the early stages of interaction with the mean shear are two-dimensional and result in the trapping of wave energy near a critical level. The subsequent dynamics of wave instability, however, are fundamentally different for two- and three-dimensional calculations. Three-dimensionality develops by transverse convective instability of the two-dimensional wave. The initially two-dimensional flow eventually collapses into quasi-horizontal vortical structures. A detailed energy balance is presented. Of the initial wave energy, roughly one third reflects, one third results in mean flow acceleration and the remainder cascades to small scales where it is dissipated. The detailed budget depends on the wave amplitude, the amount of wave reflection being particularly sensitive.

1. Introduction

The behaviour of internal gravity waves near critical levels is a problem of considerable interest to a diverse audience. Waves at critical levels exhibit the interaction of shear and buoyancy forces, fluid instability and stratified turbulence, all topics of interest to many fluid dynamicists and applied mathematicians. The interaction occurs in nature; internal waves approach critical levels as they propagate through larger-scale currents in the ocean and winds in the atmosphere. Though their detailed dynamics are not yet well understood, the behaviour of waves at critical levels is thought to be of fundamental importance. Critical-level interactions may be largely responsible for the transfer of internal wave energy to dissipation scales in the ocean interior. Oceanographic interest in particular has been stimulated by Henyey, Wright & Flatte (1984). In this work, it was shown that nearly all small-scale waves encounter a critical level within a few inertial periods when propagating through a realistic background field of internal waves.

The modification of internal waves as they propagate through an ambient shear flow is well described by asymptotic methods (Whitham 1974; Bretherton 1966) when the lengthscale of variability in the ambient shear is large compared to the wavelength and the WKB approximation is appropriate. These methods, however, break down at critical levels, where the phase speed of the wave matches the ambient flow speed, predicting infinite energy densities. Carrying the solutions to higher order to resolve the mathematical singularity necessitates the inclusion of additional physics.

Two general approaches have been taken. In the first, closure is obtained by the inclusion of molecular effects, neglecting nonlinearities. This problem has been treated numerically by Hazel (1967) and Fritts & Geller (1976). While this limit is certainly applicable in some situations, the nearly inviscid, nonlinear limit is perhaps of primary importance for many geophysical flows. In this regime, wave instability and small-scale turbulence can result from the trapping of waves at critical levels.

Though some laboratory investigations of critical level interactions have been conducted (Thorpe 1981; Koop 1981; Koop & McGee 1986), previous numerical studies have been limited to two spatial dimensions (Breeding 1971; Fritts 1982; Winters & D'Asaro 1989; Walterscheid & Schubert 1990). Constraining a problem to two dimensions, however, can produce some unexpected consequences, one example being the counter-intuitive form of wave instability exhibited in the simulations of Winters & D'Asaro (1989). As expected, large-amplitude waves produced overturned isopycnals as well as localized regions of high shear near a critical level. Rather than breaking down rapidly due to convective instability, however, the overturns were observed to persist for greater than ten buoyancy periods as the wave shear continued to intensify. Eventually, a wave instability did occur, the energetics of which were shown to be driven primarily by the wave shear rather than the available potential energy of the overturns.

In an attempt to interpret this result, Winters & Riley (1992) performed a linear stability analysis of a family of simplified velocity and density profiles similar to those produced by waves near critical levels. The study focused on the interaction between the shear and convective instability mechanisms. For spatially oscillatory profiles with both strong shear and locally unstable stratification, the type of instability predicted was found to depend strongly on the geometrical orientation of a given disturbance. For disturbances with variability in the streamwise direction, a shear-dominated instability is preferred even in the presence of overturns in the stratification, a result consistent with the two-dimensional simulations of Winters & D'Asaro (1989). Disturbances oriented in the spanwise direction, however, are unaffected by the shear and undergo a convective instability on the buoyancy timescale. The results of the stability analysis suggest that the wave instability near the critical level may have been quite different had the simulations of Winters & D'Asaro (1989) been performed in three dimensions rather than in two. Higher-resolution simulations of two-dimensional waves at critical levels have been carried out by Lin *et al.* (1993) with similar results. Lin *et al.* analysed the stability of their computed solutions directly, i.e. without simplification, and confirmed the importance of three-dimensional dynamics in the wave breakdown.

In this work, we use a three-dimensional numerical model to study the behaviour of internal waves at critical levels. We have two primary motivations in investigating the three-dimensional aspects of this problem. The first is to check the prediction of linear stability theory, namely that instability should develop through convective rolls oriented spanwise to the ambient shear. The second is to quantify the distribution of energy between various components of the flow field, i.e. the incident wave packet, the mean flow, reflected waves, mixing and dissipation. As was pointed out by Breeding (1971), the division of energy between these components may be different in three dimensions than in two.

In formulating a mathematical model to be solved numerically, we assume that, for moderately large-amplitude incident waves, an instability will occur, leading to the formation of a localized region of small-scale turbulent flow. The initial wave packet will be prescribed so that the wave envelope is slowly varying with respect to its vertical

wavelength. From linear asymptotic theory, we know that the vertical wavenumber of the waves increases dramatically through interaction with the ambient shear. Further, we expect that wave instability will produce turbulent flow at even smaller scales. Thus, the process is expected to be fundamentally scale separated, characterized by greatly disparate lengthscales.

Ideally, direct numerical simulations would be used and the numerical model would resolve the entire range of scales, from the vertical scales of the ambient shear and the packet envelope to the turbulent dissipation scales. In the ocean thermocline, the required computational bandwidth spans scales from tens or hundreds of metres to centimetres or millimetres. At present, this is not a realistic goal if three-dimensional simulations are required. As one objective is to investigate the nearly inviscid, nonlinear instability of waves near critical levels, we choose to resolve the largest scales of the problem and introduce a subgrid-scale model that rapidly damps energy at the smallest computational scales. We require that the sub-grid-scale model have minimal direct effect on motions at the scale of the wave instability. As the scale of wave breaking is not known *a priori*, some trial and error was necessary to define an adequate damping scheme. The results thus obtained belong to a class of calculations known as large-eddy simulations.

A series of calculations is presented, intended to highlight and elucidate individual processes. To quantify the nonlinear effects, i.e. the extent to which the solution does not simply scale with incident wave energy, calculations are performed for both small- and large-amplitude incident waves. The initial amplitudes are $\frac{1}{4}$ and $\frac{3}{4}$ of the amplitude required for overturning respectively. Three-dimensional aspects of the problem are examined through direct comparison of two- and three-dimensional simulations.

The numerical model and the non-dimensionalization scheme are presented in §2. Initial-value problems for wave packets approaching critical levels are defined in §3. The contrasting dynamics of unstable waves in two and three dimensions are considered in §4. An important dynamical mode, the potential vorticity carrying vortical mode, can emerge when the problem is treated in three rather than in two dimensions. The dynamics of potential vorticity are also discussed in §4. A detailed energy analysis, quantifying the distribution of energy between the various flow components, is presented in §5. A discussion and summary of results is provided in §6.

2. Numerical model

The dimensionless equations of motion for a density-stratified Boussinesq fluid are listed below.

$$\frac{\partial \boldsymbol{u}}{\partial t} + \boldsymbol{u}\cdot\nabla\boldsymbol{u} + Ri\,\rho'\hat{z} = -\nabla p + \mathscr{D}[\boldsymbol{u}], \tag{1}$$

$$\frac{\partial \rho'}{\partial t} + \boldsymbol{u}\cdot\nabla\rho' - w = Pr^{-1}\,\mathscr{D}[\rho'], \tag{2}$$

$$\nabla\cdot\boldsymbol{u} = 0. \tag{3}$$

Here $\boldsymbol{u} = [u, v, w]$ are the velocity components in the $\hat{x}$-, $\hat{y}$- and $\hat{z}$- (vertical) directions respectively. The primes in (1) and (2) indicate perturbations from the background potential density profile $\bar{\rho}(z)$. The magnitudes of the perturbations are arbitrary; no small-amplitude approximations are made. The linear operator $\mathscr{D}$ determines the dissipative and diffusive behaviour of the flow at small scales; $\mathscr{D}[f] = Re^{-1}\nabla^2 f$.

The velocity and length scales used in the non-dimensionalization are $U = 1$ cm s^{-1} and $L = 7.5$ m respectively. These scales correspond to the horizontal phase speed of

the incident wave packet and the approximate vertical scale of the waves just prior to instability near the critical level. Density perturbations ρ' are scaled by $L|\mathrm{d}\bar{\rho}/\mathrm{d}z|$. The density gradient is chosen to give a buoyancy frequency $N = 3.8$ c.p.h. where $N^2 = (-g/\rho_0)\,\mathrm{d}\bar{\rho}/\mathrm{d}z$, g is the gravitational acceleration and ρ_0 is the characteristic density. This value is typical of the upper ocean thermocline. The time t is scaled by L/U and pressure p by $\rho_0 U^2$.

Three dimensionless parameters appear in the equations of motion. The bulk Richardson number $Ri = [NL/U]^2$ relates the wave scales to the ambient stratification. All calculations reported were run with $Ri = 25$. The remaining two dimensionless parameters, the Reynolds number $Re = UL/\nu$, and the Prandtl number $Pr = \nu/\kappa$ control the rates of molecular dissipation and diffusion. The equations are solved over the cube $(x, y, z) \in [0, 10)$. Periodic boundary conditions are imposed in each direction and standard pseudospectral numerical techniques are employed.

Given existing computational constraints, a three-dimensional numerical model cannot resolve both the outer scales of the problem and the dissipation scales. Truncating the bandwidth of a computational model, however, results in numerical stability problems when energy is transferred to small scales. One approach to maintaining stability is to perform low-Reynolds-number simulations. For the problem treated here, however, Reynolds numbers small enough to preserve numerical stability result in excessive damping of the wave packet as it approaches the critical level. Wave instability is then viscously prohibited.

To overcome this difficulty, a subgrid-scale model is introduced. For purely numerical reasons, the operator $\mathscr{D}$ is replaced with higher-order derivatives; $\mathscr{D} = (1/Re')\nabla'^6$. The prime associated with the Reynolds number indicates that its meaning (and that of Pr) should be reinterpreted, in order to maintain dimensional consistency. The basic operator

$$\nabla'^2 = \alpha^2 \frac{\partial^2}{\partial x^2} + \beta^2 \frac{\partial^2}{\partial y^2} + \frac{\partial^2}{\partial z^2}$$

is anisotropic, allowing stability to be preserved under non-uniform discretization. The constants α and β define the degree of anisotropy and have been set to n_z/n_x and n_z/n_y respectively where $n_x = n_y = 32$ and $n_z = 200$ are the number of grid points in the $\hat{x}$-, $\hat{y}$- and $\hat{z}$-directions.

High-order dissipation operators are more frequently used for large-scale ocean models but have also been used at small scales (Farge 1987). The advantage of such a scheme is that, by tuning the coefficients and the derivative orders, dissipation and diffusion can be constrained to a very narrow band of computational wavenumber space, leaving the remainder to be treated essentially inviscidly and non-diffusively. For sixth-order derivatives and the grid resolution stated above, the values $Re' = 2.66 \times 10^9$, $Pr = 1$ were found to minimally damp the energy cascade to small scales. The damping scheme is easily implemented using spectral methods. Qualitatively, this approach is supported by the work of Domaradzki *et al.* (1987) who compared low- and high-resolution simulations of isotropic turbulence. The form of sub-grid-scale parameterization required for the calculations to agree at overlapping scales was then determined. It was found that low-resolution simulations should rapidly damp energy only in a narrow band of scales near the resolution limit.

For the three-dimensional, large-amplitude simulation discussed in this paper, wave instability occurs prior to appreciable dissipation or diffusive mixing. As will be shown in §5, approximately 95% of the kinetic energy dissipation occurs after the mode of instability has become well established. Thus, the subgrid-scale dissipation model has

minimal direct effect on the wave instability. The primary role of the subgrid-scale model is to rapidly damp the subsequent cascade of energy to small scales. Assuming that motions at subgrid scales do not significantly influence the flow at resolved scales, the overall rates of dissipation and mixing are determined by the rates of energy transfer downscale, i.e. by processes occurring at well resolved scales in the nearly inviscid limit.

3. Initial conditions

For simple periodic boundary conditions, in the absence of external forcing, the initial conditions determine the mathematical problem for the model described in §2. Although our interest is primarily in the behaviour of large-amplitude waves in three dimensions, several initial-value problems have been solved numerically, with each calculation isolating a particular aspect of the physics. Through a series of calculations, we will contrast the behaviour of two- and three-dimensional waves as well as linear and nonlinear dynamics. The initial conditions for these calculations are given here. All variables discussed in this and subsequent sections are dimensionless, with the scaling of variables given in §2.

Typically, the initial conditions consist of a one-dimensional ambient shear flow, $U(z)\,\hat{\boldsymbol{x}}$, and a two-dimensional internal wave packet comprising density perturbations and velocity components in the $\hat{\boldsymbol{x}}$- and $\hat{\boldsymbol{z}}$-directions. Note that the prescribed wave packets have no variability in the $\hat{\boldsymbol{y}}$-direction, spanwise to the ambient shear. For these initial conditions, the flow remains strictly two-dimensional at all subsequent times. If, however, an additional initial component is prescribed that has variability in the spanwise direction, the flow is free to evolve in three dimensions. In particular, we wish to allow this degree of freedom to nonlinear waves as they are about to break down near a critical level. Thus, for most of the calculations, we also prescribe a weak, three-dimensional 'noise' field. The energy spectrum of the noise is white. The phases between velocity and density perturbations were chosen randomly, with incompressibility imposed explicitly for each Fourier mode. Although each of the calculations presented was carried out in three dimensions, a distinction is made between a two-dimensional calculation, which is initialized with no noise and hence remains two-dimensional, and a three-dimensional calculation, for which a noise field is prescribed.

The analytic forms (4)–(7) for the initial wave packets are obtained by taking an unbounded, free internal wave solution and multiplying each component by an envelope function that varies only slowly in the vertical direction. An additional velocity component must be added to ensure incompressibility, but this component is small in amplitude, being proportional to the ratio of lengthscales of the wave and its envelope. The result is

$$\rho'(\boldsymbol{x},0) = A(z)\cos(kx+mz), \tag{4}$$

$$w(\boldsymbol{x},0) = \omega A(z)\sin(kx+mz), \tag{5}$$

$$u(\boldsymbol{x},0) = -\frac{m\omega}{k}A(z)\sin(kx+mz)+\frac{\omega}{k}A'(z)\cos(kx+mz), \tag{6}$$

$$v(\boldsymbol{x},0) = 0. \tag{7}$$

The frequency ω satisfies the linear dispersion relation in the absence of a mean flow: $\omega^2 = Rik^2/(k^2+m^2)$. The wave envelope is prescribed by setting

$$A(z) = A_0\,\mathrm{e}^{-(0.255z-10])^2}. \tag{8}$$

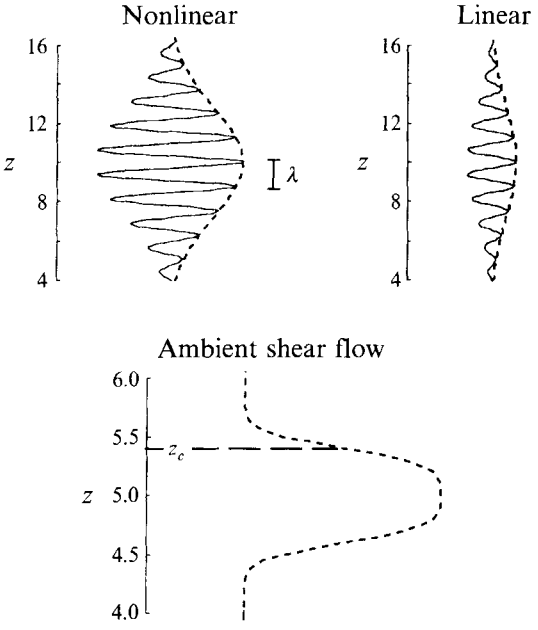

FIGURE 1. The location and relative scales associated with the wave packets and the ambient shear flow. With respect to the initial vertical wavelength λ, the wave envelope varies slowly and the distance to the critical level z_c is moderately large.

The polarization of the wave components is chosen so that the packets propagate downward. The wavenumbers k and m are set equal to $(2\pi)/10$ and $8\times(2\pi)/10$, corresponding to horizontal mode 1 and vertical mode 8 respectively. The packets are initially located in a region of the domain where the ambient shear is negligible, and subsequently propagate into the interaction region where the shear becomes important. The total distance the peak of the packet envelope must travel before encountering the critical level is large compared to the initial vertical wavelength.

In distinguishing between calculations, we will use the modifiers *linear* and *nonlinear*. It should be understood that the distinction refers only to the initial amplitudes of the wave packets; the equations solved numerically are fully nonlinear in all cases. The nonlinear calculations have wave amplitudes three times, and energies nine times, those of the linear calculations. The value of A_0 is 0.75 and 0.25 for the nonlinear and linear calculations respectively.

Given the characteristic parameters of the incident wave packet, a shear flow can be prescribed so that the waves will encounter a critical level at a known location. A depth-dependent shear flow is specified with a peak amplitude slightly greater than twice the critical speed for the given wave packet.

$$U(z) = C_p[2.1\,\mathrm{e}^{-(2.26[z-5])^4} - 1]. \tag{9}$$

The shear flow itself is stable to Kelvin–Helmholtz-type instabilities (Drazin & Reid 1981), and has a gradient Richardson number $Ri_g = Ri/(\mathrm{d}U/\mathrm{d}z)^2 = \frac{1}{2}$ at the critical level. The reference frame of the calculation is set by adding a spatially uniform component $-C_p = -\omega/k$ to (9). In this frame, the Eulerian phase speed and hence the critical flow speed are both zero. Figure 1 shows the relative scales associated with the wave packets and the ambient shear flow.

4. Dynamics of wave instability

4.1. *Overview*

Here and in subsequent sections we will confine our attention to the flow field within the subdomain $5 \leqslant z < 7.5$, where the wave packets interact with the ambient shear flow. The flow outside this region consists primarily of a freely propagating incident wave packet, though reflected waves are also present during the later stages of the calculations. For the purpose of this analysis, the wave propagation in these regions is not of interest.

Figure 2 shows contours of the density field in the depth–time plane for the three-dimensional linear, and the two- and three-dimensional nonlinear calculations. This view of the flow corresponds to that obtained by a vertical profiler moving uniformly in the direction opposing the intrinsic phase speed of the wave. This reference frame is convenient here as several wavelengths can be displayed within a reasonably short time window, allowing changes in phase direction to be perceived easily. For illustration, the region where the mean horizontal flow is greater than or equal to the critical speed is shaded.

Prior to about $t = 10$ (time is given in buoyancy periods), most of the isopycnal displacements occur above the interaction region. Lines of constant phase can easily be distinguished and remain approximately parallel to one another as the waves propagate freely. Note that the critical level z_c moves upward in time, particularly in the nonlinear cases, as indicated by the widening shaded region. Just above the shaded region, the ambient shear is non-zero but the flow speed is less than the critical value. In this region, the orientation of the phase lines rotates clockwise, indicating a slowing of the downward wave propagation. Near the critical level, i.e. near the top edge of the shading, the displacements become large, beginning about $t = 15$, as more of the wave energy becomes trapped. Well below the initial location of the critical level, the isopycnal disturbances remain small in all cases, indicating very little transmission of wave energy.

In the linear calculation (*a*), the displacements never become so large that gravitationally unstable density gradients occur. After about $t = 30$, the displacements near the critical level gradually decrease with time. Well above the critical level, a standing wave pattern is apparent, indicating reflection of waves away from the vicinity of the critical level. Significant wave reflection was also observed by Breeding (1971) for waves at critical levels when the gradient Richardson number was less that about 2.

While the overall evolution of the flow in the nonlinear calculations (*b*) and (*c*) is similar, the results are markedly different near the critical level where the wave amplitudes are largest. Overturns in the isopycnals appear near the critical level beginning at about $t = 20$ for both the two- and three-dimensional cases. The location of the largest overturns moves upward in time, following the critical levels as it moves toward the wave source. While these features persist until about $t = 40$ in the two-dimensional case, they are no longer present after about $t = 22$ in the three-dimensional calculation. After the disappearance of these overturns, the flow becomes nearly quiescent at the original level of these features. The isopycnal spacing in this region, however, has increased, suggesting diapycnal mixing. This is most evident in the three-dimensional case but can also be seen in the later stages of the two-dimensional case.

4.2. *Streamwise view*

We now look at the flow near the critical level in more detail. Recall that the initial wave packets were uniform in the direction spanwise to the ambient shear flow and that

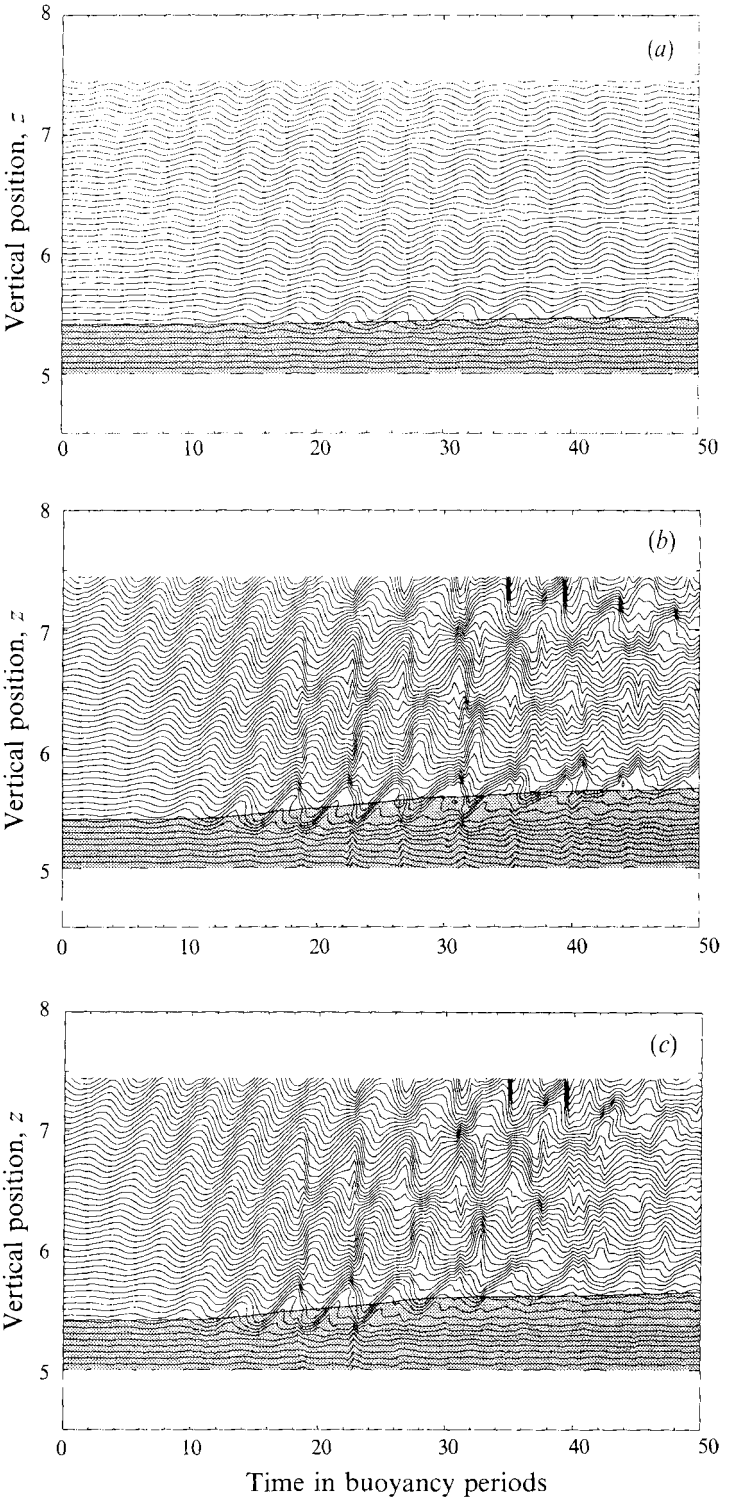

FIGURE 2. Density contours in the depth–time plane for (*a*) the three-dimensional linear, (*b*) the two-dimensional nonlinear, and (*c*) the three-dimensional nonlinear calculations. Vertical profiles of density are sampled at $y = 2.5$ and at $x = x_0 - \gamma t$ with $\gamma = \frac{3}{4}$.

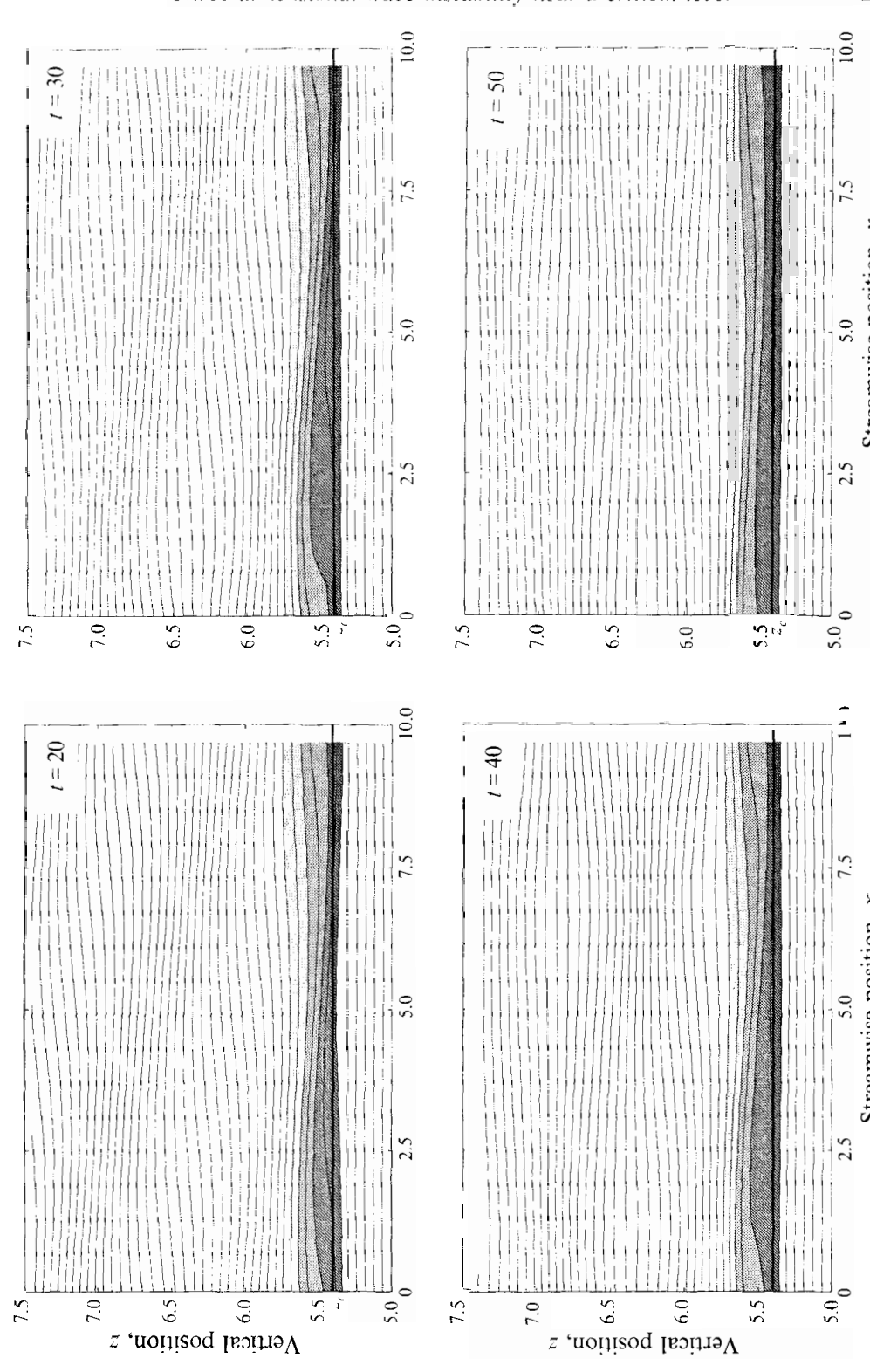

FIGURE 3. Density contours (linear calculation) in the $y = 0$ plane at $t = 20$, 30, 40 and 50 buoyancy periods. Contour increment is 0.06. The shading indicates the region near the critical level z_c where the wave energy density increases and the largest displacements occur.

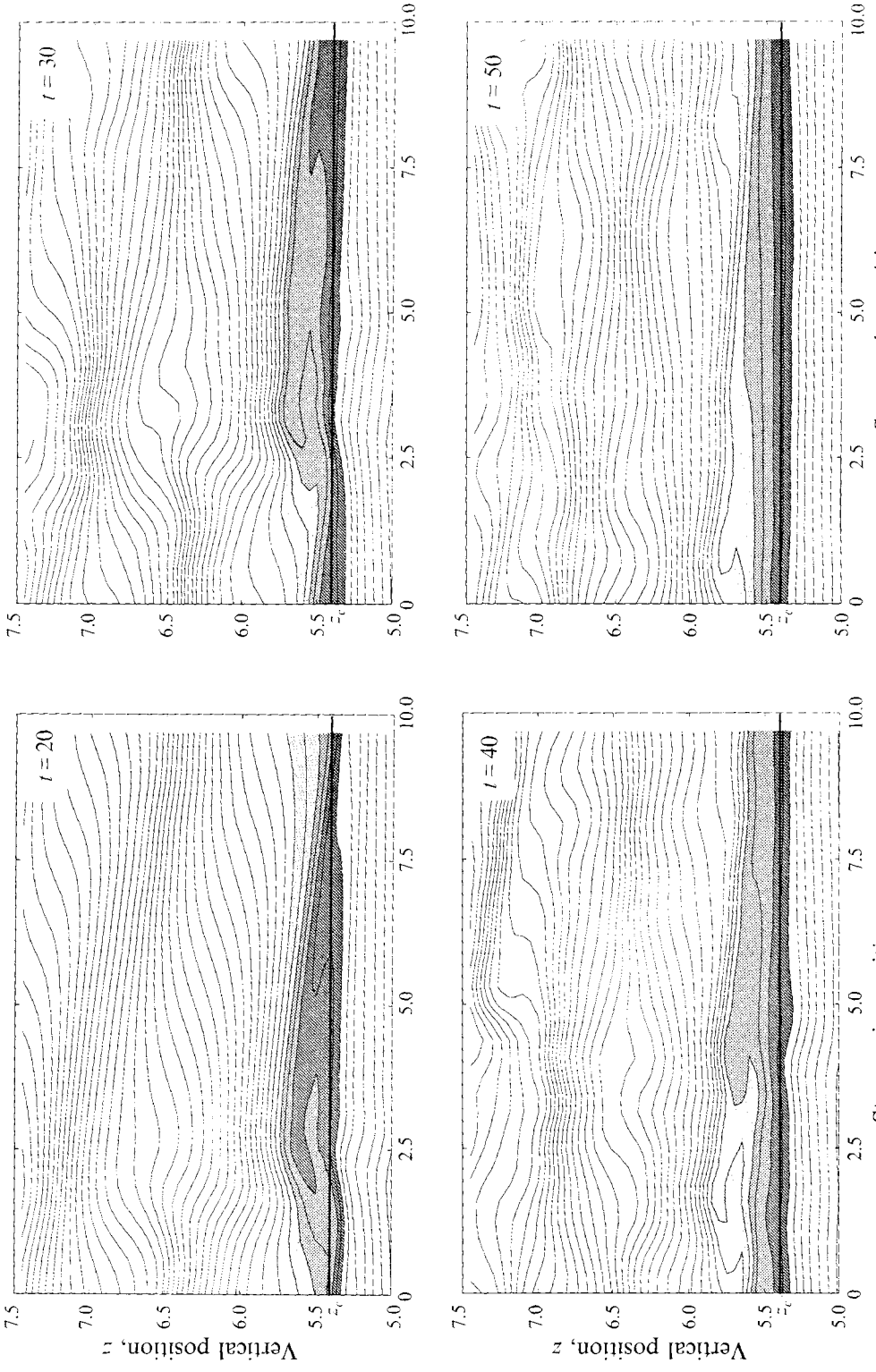

FIGURE 4. Density contours in the $y = 0$ plane for two-dimensional large-amplitude wave packets (nonlinear calculation) at $t = 20$, 30, 40 and 50 buoyancy periods. Contour increment and shading are the same as in figure 3.

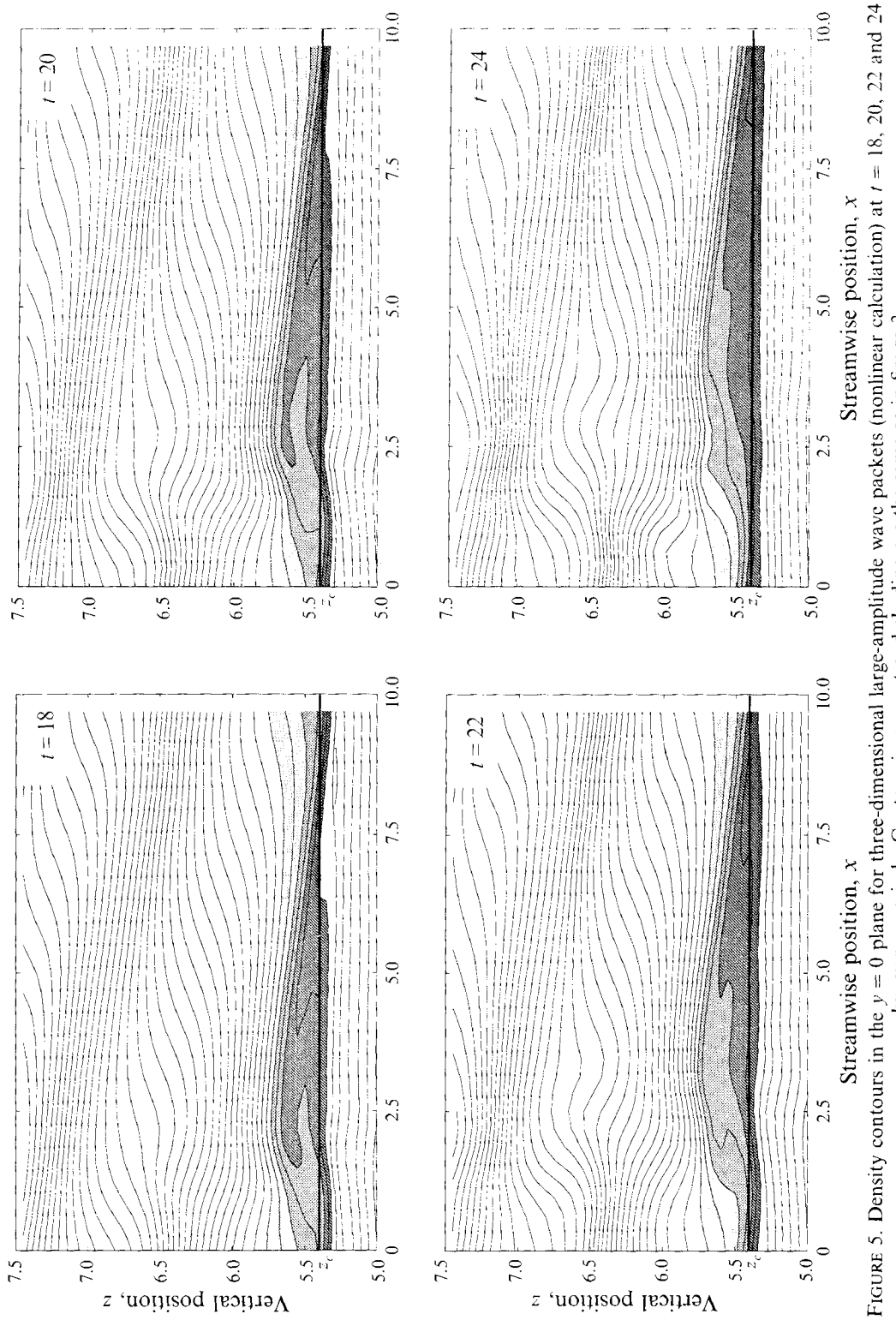

FIGURE 5. Density contours in the $y = 0$ plane for three-dimensional large-amplitude wave packets (nonlinear calculation) at $t = 18$, 20, 22 and 24 buoyancy periods. Contour increment and shading are the same as in figure 3.

the reference frame of the calculations is such that the incident packets have zero Eulerian phase speed. The overturning waves near the critical level are thus stationary. We first examine their development in time in the streamwise (x, z)-plane. The results are strictly independent of spanwise position y for the two-dimensional calculation, very nearly independent of y for the three-dimensional linear case, and exhibit regular spanwise variability for the three-dimensional nonlinear calculation.

For the linear calculation, figure 3 shows isopycnals in the (x, z)-plane, for $y = 0$, at several points in time. The largest displacements occur in the shaded region near the initial location of the critical level $z_c = 5.4$. The wave becomes moderately steep, especially at $t = 30$, but then relaxes slowly without developing any gravitationally unstable overturns. The timescale of the relaxation is relatively large, on the order of 20 buoyancy periods. There is no indication of any wave instability or sudden change in the character of the flow. The primary dynamical balance is between an energy flux toward the critical level, the transfer of energy to the mean flow and laminar dissipation. (A more detailed discussion of the energy balance is given in §5.)

The isopycnals for the two- and three-dimensional large-amplitude packets at the same spatial location are shown in figures 4 and 5 respectively. Again, the largest displacements occur in the shaded regions. For these two cases, however, the wave is energetic enough to overturn the isopycnals, creating regions where heavy fluid has been lifted above lighter fluid. Comparing figures 4 and 5 it is evident that the two flows are nearly identical at $t = 20$, with a single overturning structure appearing as the dominant feature. This suggests that the wave-like aspects of the problem, i.e. the wave propagation, its trapping and intensification to the point of overturning, are fundamentally two-dimensional. These processes exhibit no tendency to create spanwise variability in the flow. The fate of the overturning feature, however, is clearly dependent on the number of spatial dimensions it is free to evolve in. In the two-dimensional case, the overturning persists for more than 20 buoyancy periods, with no evidence of convective instability, as wave energy continues to impinge on the critical level. This behaviour is similar to that seen in Winters & D'Asaro (1989). In contrast, for the three-dimensional case, only a small amount of overturning is left by $t = 22$. No overturns are present by $t = 24$. The dynamics resulting in the gravitational stabilization of overturned waves are clearly different in three dimensions than in two. At issue is the extent to which the differing dynamics affect the ultimate distribution of incident wave energy between reflection, transmission, acceleration of the mean flow, diffusive mixing and dissipation. This is addressed, within the limitations of the large-eddy simulation approach, in §5.

4.3. *Spanwise view*

Linear stability theory predicts different dynamics for overturned waves in two and three dimensions. Winters & Riley (1992) showed that the presence of strong shear can inhibit the development of convective restratification of overturns in two dimensions. The directional dependence of the instability mechanism stems from the decreasing influence of shear on disturbances with horizontal wavenumber vectors rotated away from the streamwise direction. In the limit of orthogonally oriented disturbances, the influence of the shear vanishes, leaving only the overturned stratification to drive an instability. Thus, convective instability is predicted for overturned waves, with the fastest growth rates associated with convective cells oriented in the spanwise plane. By spanwise orientation, we mean convective cells with vorticity vectors pointing in the positive or negative streamwise direction.

To assess the development of the instability in the spanwise dimension, the simulated

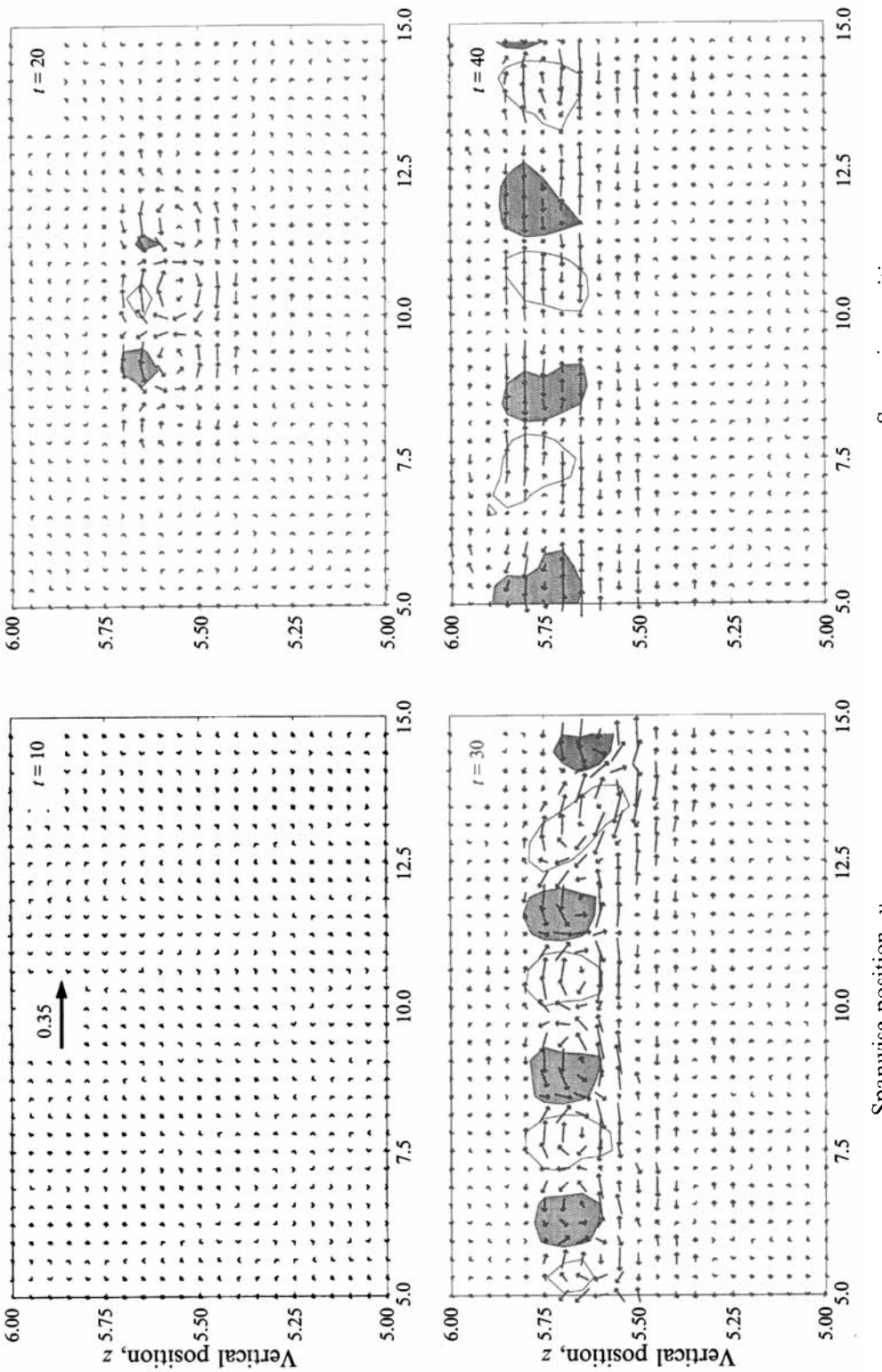

FIGURE 6. Velocity arrows of the filtered field $\boldsymbol{u}_f$ displayed in the (y,z)-plane at $x = 2.5$ *at* $t = 10$, 20, 30 and 40 buoyancy periods. Dark and light shaded regions indicate positive and negative potential vorticity Π respectively.

flow fields from the three-dimensional cases were spectrally filtered, retaining the component of the flow with mode numbers $10l/2\pi > 2$, where l is the wavenumber in the transverse $\hat{y}$-direction. The resulting velocity field is denoted $\boldsymbol{u}_f$. As the initial wave packet and the ambient shear flow were prescribed independent of y, only the small-amplitude noise field contributes to $\boldsymbol{u}_f$ initially. The magnitude of $\boldsymbol{u}_f$ remains comparable to its initial value in the linear calculation, implying that the flow remains almost entirely two-dimensional. Only the result of the three-dimensional nonlinear calculation is of interest here.

Figure 6 shows the velocity arrows of the $\hat{y}$- and $\hat{z}$-components of $\boldsymbol{u}_f$ before ($t = 10$), during ($t = 20$ and 30), and after ($t = 40$) the wave breaking event. The shading indicates regions of positive and negative potential vorticity and will be discussed in §4.4. At $t = 10$, the spanwise flow is very weak and exhibits no obvious spatial structure. By $t = 20$, however, this flow has been greatly enhanced in a localized region corresponding to the overturns in the density field. Within this region, a series of counter-rotating vortices is evident. The flow is similar in appearance to the convective cells predicted by linear stability theory. Because the noise field is initially broad-banded, the observed scale of the convective cells is, apparently, the fastest growing scale, though no calculations have been attempted to predict this scale *a priori*. By $t = 30$, convective cells have been formed throughout the horizontal extent of the computational domain. The cells have moved upward, following the overturns in the density field. By $t = 40$, the cells have moved up further and collapsed, becoming almost purely horizontal motions. Remnants of the cellular structure are still present, with the counter-rotating vortices replaced by alternating regions of convergence and divergence.

4.4. *Generation of potential vorticity*

Though potential vorticity dynamics have long proven useful in the study of large-scale geophysical flows, only more recently (Staquet & Riley 1989*a*, *b*) has potential vorticity dynamics been used in the study of stratified flows at smaller scales. This stems in part from laboratory evidence that the decay or collapse of stratified turbulence is related to the generation of quasi-horizontal pancake motions, i.e. vortical modes, but also because of the intimate connection between the generation of potential vorticity and the molecular effects of mixing and dissipation.

In a non-rotating coordinate system, potential vorticity Π is defined by $\Pi = \boldsymbol{\omega}\cdot\boldsymbol{\nabla}\rho$, where ρ is the total density $\bar{\rho}(z)+\rho'$. The conservation of Π, often referred to as Ertel's theorem, is expressed as

$$\frac{\partial \Pi}{\partial t} + \boldsymbol{u}\cdot\boldsymbol{\nabla}\Pi = (Pr\,Re)^{-1}\boldsymbol{\omega}\cdot\boldsymbol{\nabla}\nabla^2\rho + Re^{-1}\,\boldsymbol{\nabla}\rho\cdot\nabla^2\boldsymbol{\omega} \tag{10}$$

(see e.g. Lelong 1989). Equation (10) states that, following the fluid motion, potential vorticity can be changed only through molecular effects. An analogous equation, with higher-order spatial derivatives on the right-hand side, can be derived for flows satisfying equations with higher-order dissipation operators. Integrating (10) over a volume enclosed by isopycnals reveals that the integrated Π is identically conserved even in a viscous, diffusive flow. This does not imply, however, that no changes in the Π-field occur. Potential vorticity variance can increase (or decrease) substantially.

For the problem studied here, it should be noted that neither the initial wave packet nor the ambient shear flow carry potential vorticity. The vorticity of the noise field in the three-dimensional simulations is randomly oriented and so these calculations do contain a small amount of potential vorticity initially. The three-dimensional linear

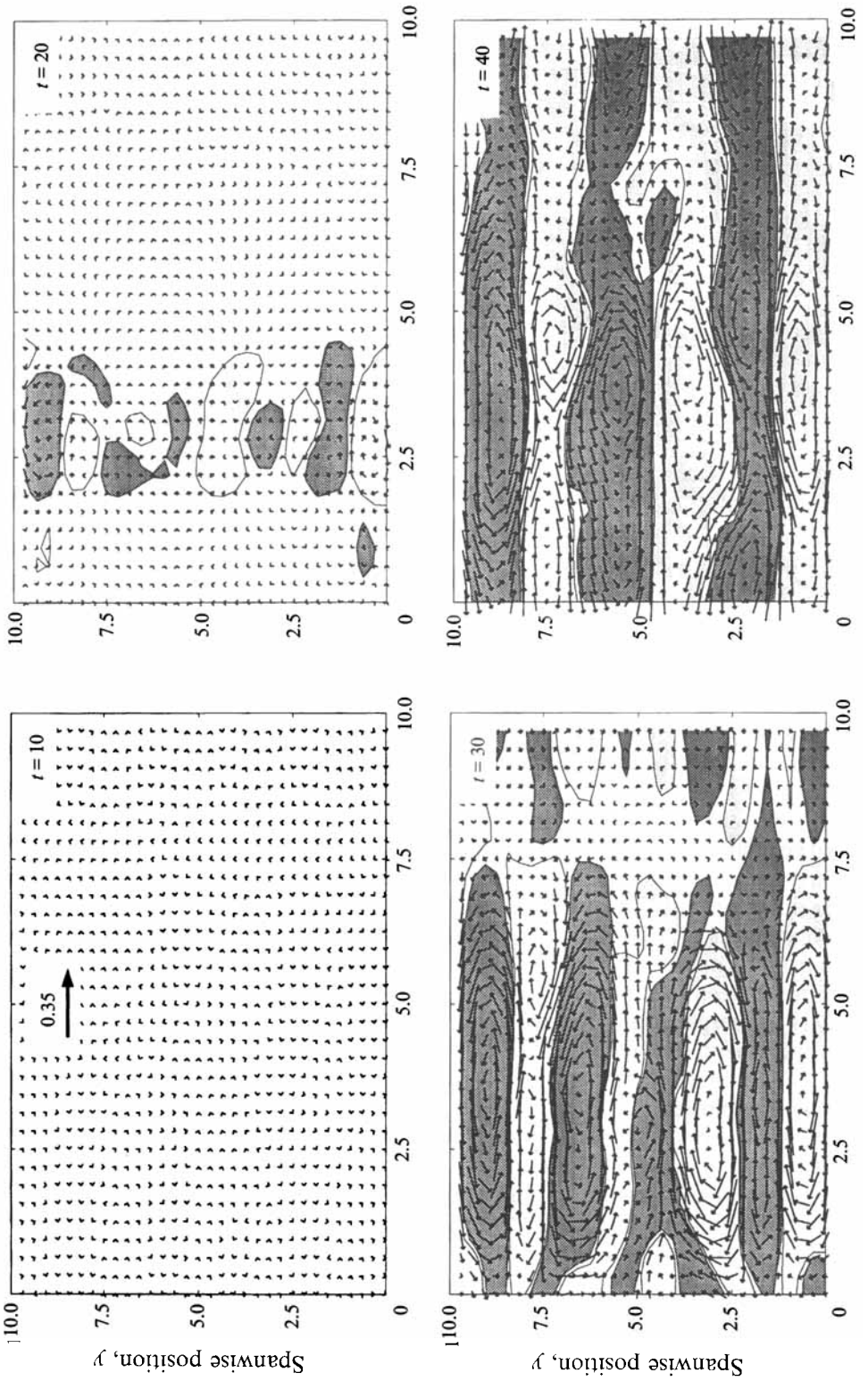

FIGURE 7. Velocity arrows associated with the leading-order approximation of $\boldsymbol{u}_\pi$ and contours of the vertical vorticity. After $t = 30$, the isopycnals are nearly flat and so $\boldsymbol{u}_{\pi 0}$ and vertical vorticity are very good approximations of the potential vorticity carrying flow.

case developed no significant three-dimensionality and no significant potential vorticity signal. We therefore focus our attention on the potential vorticity dynamics of the three-dimensional nonlinear case.

The potential vorticity Π can be calculated directly from the computed flow fields. Regions of high potential vorticity magnitude are correlated with the formation of the transverse vortices, as shown in figure 6. To get a better feel for this flow component, we also estimate the velocity field $\boldsymbol{u}_\pi$, associated with the potential vorticity. In the later stages of the simulation, the characteristic slope of the isopycnals is small. As a result, the leading-order term in the expansion of $\boldsymbol{u}_\pi$ for large Richardson numbers is a good approximation (Lelong 1989). This leading-order term $\boldsymbol{u}_{\pi 0}$, is simply the velocity field associated with the vertical vorticity $(\boldsymbol{\omega}\cdot\hat{\boldsymbol{z}})$. Velocity arrows for $\boldsymbol{u}_{\pi 0}$ are shown in figure 7. The horizontal plane of this figure is $z = 5.7$, which is located in the region of convective activity.

At $t = 10$ there is only a very weak vertical vorticity signal with no evidence of spatial coherence. By $t = 20$, when the spanwise convective cells are well established (see figure 6), alternating regions of horizontally circulating flow have begun to develop. By $t = 30$, the isopycnals at this level are nearly flat and the vertical vorticity is a very good approximation of the potential vorticity. The flow pattern evident earlier has been significantly enhanced and covers nearly the full extent of the streamwise direction by $t = 40$. Note that the transverse spatial scale of the horizontal vortices at $t = 30$ and 40 is approximately equal to the scale of the convective cells in figure 6. Further, the orientation of the circulation patterns is consistent with rotation of the convective cells into the horizontal plane by the ambient shear. From figures 6 and 7 we see that by $t = 40$ the flow consists of nearly horizontal rotational motions. These motions are localized in depth, confined to the region of wave instability.

The spatial relationship between potential vorticity $\Pi = \boldsymbol{\omega}\cdot\nabla\rho$ and the overturning wave can also be seen in figure 8. Potential vorticity is first produced near the tip of the overturning feature. While the general trend of the development can be inferred from figure 8, three-dimensional animations of this process were much more revealing. Potential vorticity tubes appeared to stream out from the crests of the overturns, falling downward into the troughs. These tubes of potential vorticity alternate in sign in the spanwise direction, and are approximately aligned with the cores of the convective cells as shown in figure 6.

Aside from a kinematic relationship, there appears to be further indication of a close connection between the onset of spanwise convection and the production of potential vorticity. The energetics of these two flow components evolve nearly in parallel. Figure 9 shows the kinetic energy content of $\boldsymbol{u}_\pi$ and the filtered velocity field $\boldsymbol{u}_f$ as functions of time. For comparison of magnitudes, the vertical kinetic energy, indicative of wave activity, is also plotted.

The kinetic energy of both $\boldsymbol{u}_\pi$ and $\boldsymbol{u}_f$ increases sharply at about $t = 20$, after the instability has developed. Both quantities then remain approximately constant. By the end of the simulation, the kinetic energy content of the potential vorticity field is nearly an order of magnitude greater than the vertical kinetic energy of the internal wave field. (Though not apparent in figure 9, most of the wave kinetic energy is associated with horizontal motions by this point.) Estimating the final wave energy to be twice the final available potential energy (see § 5), the ratio of vortical mode energy to wave energy is approximately $\frac{1}{4}$. The buoyant collapse of turbulence into vortical motions may be an intrinsic process associated with stratified flows. The collapse of stratified turbulence into a flow field with an energetic vortical mode component and a much weaker internal wave signature has also been observed in numerical simulations of

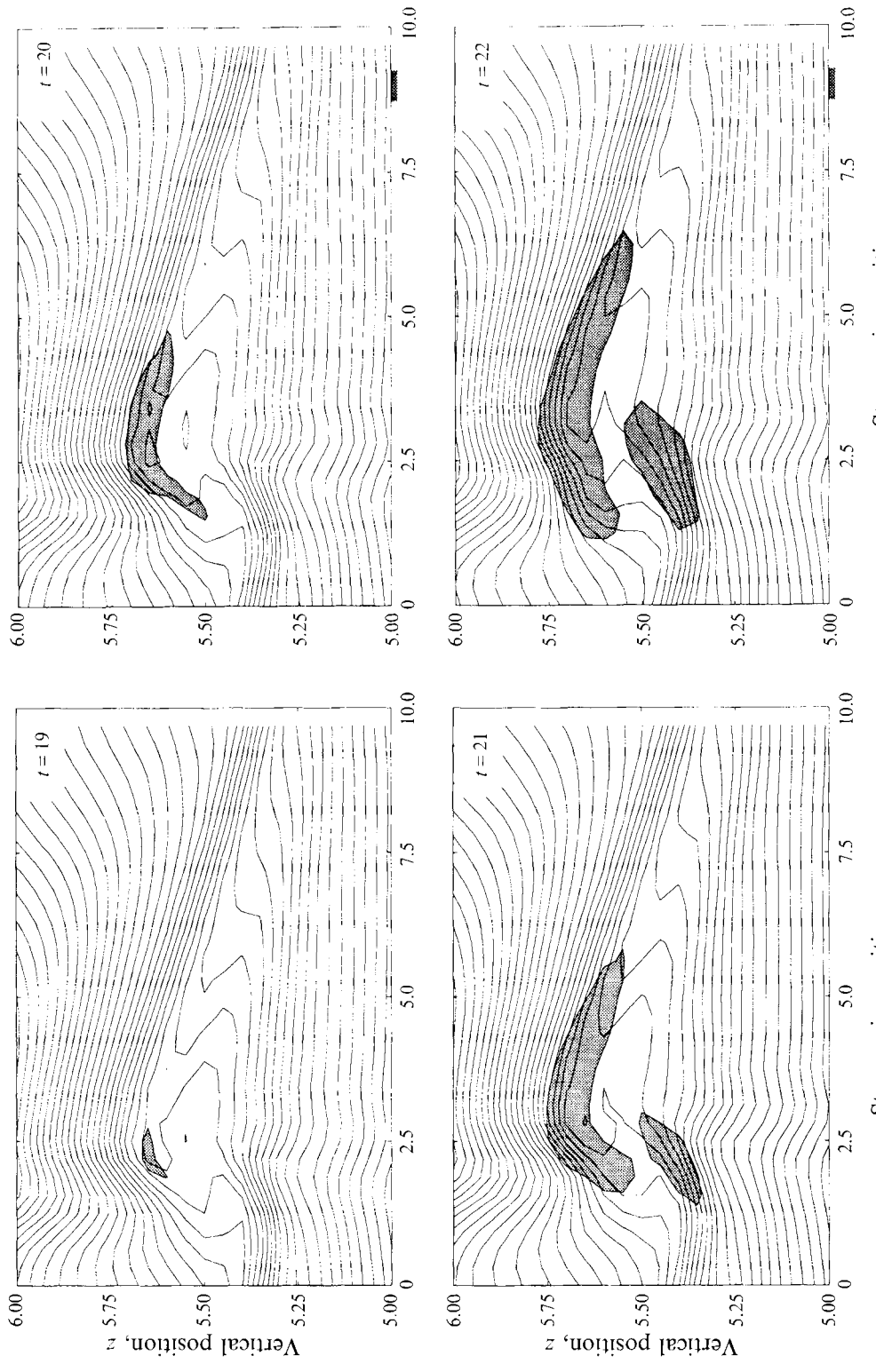

FIGURE 8. Expanded view of overturning waves near the critical level. Contours of ρ are shown in the $y = 0$ plane. Shaded regions highlight the generation of potential vorticity Π.

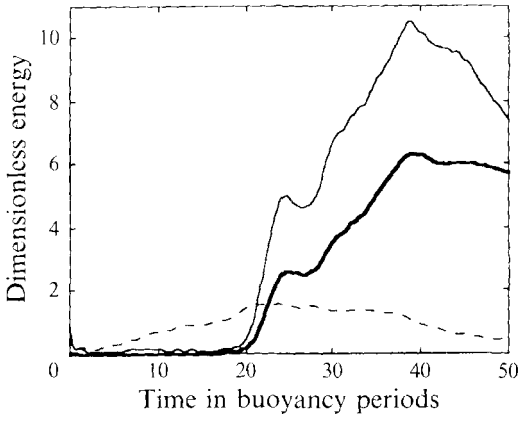

FIGURE 9. Energy growth of the velocity fields associated with potential vorticity and the spanwise flow. The horizontal kinetic energy of $\boldsymbol{u}_\pi$ (——), the kinetic energy of $\boldsymbol{u}_f$ (– – –) and the total vertical kinetic energy (----) are shown.

Kelvin–Helmholtz instabilities (Staquet & Riley 1989*a*). This collapse has also been observed in the laboratory under conditions of strong stratification (Lin & Pao 1979).

The dynamics of wave instability near critical levels has been shown to be fundamentally different in two and three dimensions when the energy of the incident wave is large enough to produce overturns in the stratification. Convective instability in a mode periodic in the spanwise direction provides the mechanism by which the flow becomes three-dimensional. The timescale of wave breakdown depends strongly on the mechanism of instability, being far longer in the two-dimensional calculation, in which spanwise convection cannot develop. The numerical results in three dimensions are consistent with the predictions of linear stability theory (Winters & Riley 1992; Lin *et al.* 1993).

4.5. *Numerical resolution of instability*

Figure 10(*a*) shows the displacement power spectra E_ζ at $t = 20$ and 22 as functions of vertical mode number $10m/2\pi$, where m is the vertical wavenumber. The spectra have been averaged over horizontal wavenumbers and scaled by the maximal value. The unstable internal wave packet contains most of the energy and is centred at approximately mode 10. Between times 20 and 22, the energy of the modes of instability, i.e. the convective cells shown in figure 6, rapidly increases. The spatial scales associated with the growing instability are highlighted. A characteristic vertical mode number of the instability is 28, as shown in the figure. For a spectral model with $n_z = 200$ vertical grid points, 101 vertical modes can be represented numerically. The vertical scales of the instability are well within the resolution of the numerical model.

Figure 10(*b*) shows the horizontal kinetic energy spectra, E_{hke}, computed using the flow field shown in figure 7 at $t = 20$. The spectra are plotted in area-preserving form, normalized by the power at streamwise mode zero. The solid curve is the spectrum as a function of spanwise mode number $10l/2\pi$, averaged over $x \in [0, 10)$. This spectrum is clearly peaked, with a dominant spanwise mode number of 5. The broken curve is the streamwise mode number spectrum averaged over $y \in [0, 10)$. Most of the energy is in the lowest few modes.

Given the spatial scales at which the instability occurs, it is important to examine the effect of the subgrid-scale dissipation model at these scales. A dimensionless viscous timescale t_ν can be defined as a function of the wavenumbers k, l and m. For a direct numerical simulation $t_\nu = Re/(k^2 + l^2 + m^2)$. For the subgrid-scale model defined in §2,

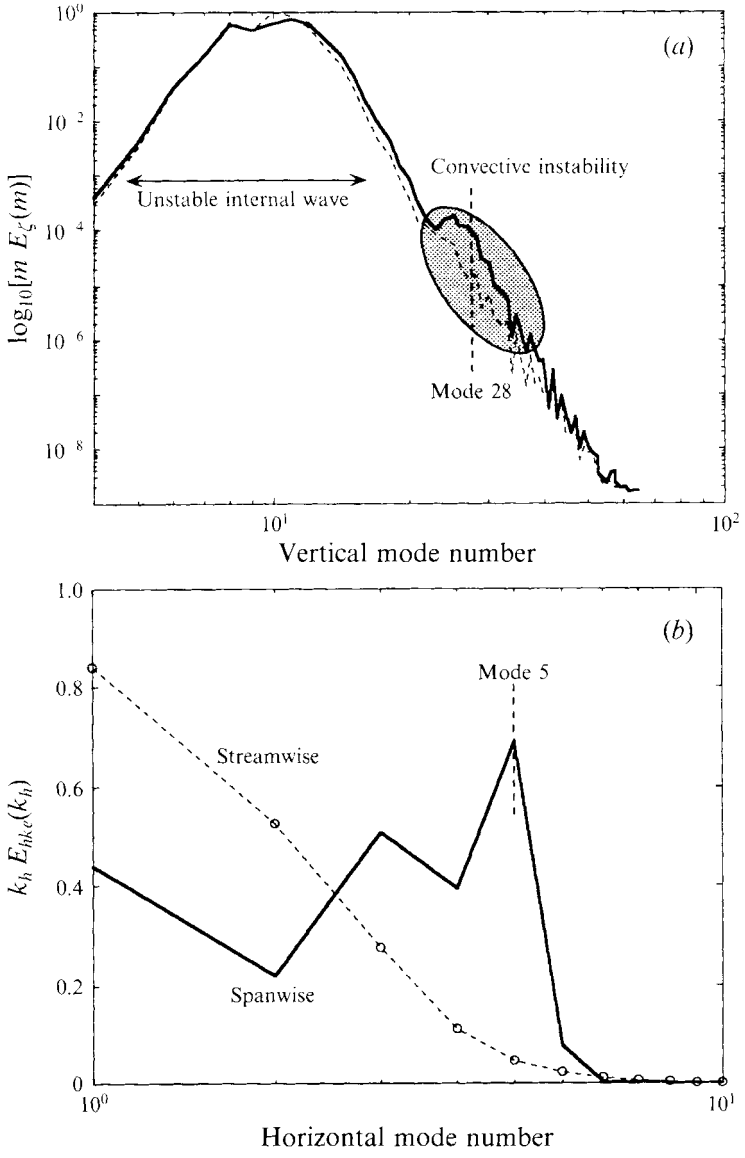

FIGURE 10. (*a*) Displacement power spectra E_ζ at $t = 20$ (----) and 22 (——). The transverse mode of convective instability grows rapidly between times 20 and 22 and has a characteristic vertical mode number of 28. (*b*) Horizontal kinetic energy spectra, E_{khe}, computed using the flow field shown in figures 6 and 7 is 5.

$t_\nu = Re'/(\alpha^2k^2+\beta^2l^2+m^2)^3$. Defining the dimensionless buoyancy timescale $t_{bv} = Ri^{-\frac{1}{2}}$, the ratio t_{bv}/t_ν can be examined as a function of wavenumber. Figure 11 shows this ratio, computed for both normal viscosity and the hyperviscosity described in §2, as a function of streamwise mode number $10k/2\pi$. The viscous timescales were computed using the observed characteristic scales of the instability, i.e. for a spanwise mode number of 5 and a vertical mode number of 28. The displacement power spectrum, calculated using the data from figure 8 at $t = 21$, is also shown in area-preserving form. Nearly all the energy associated with the wave instability occurs at scales for which $t_\nu \gg t_{bv}$. Note that for a low-*Re* direct simulation, viscous damping would occur on the

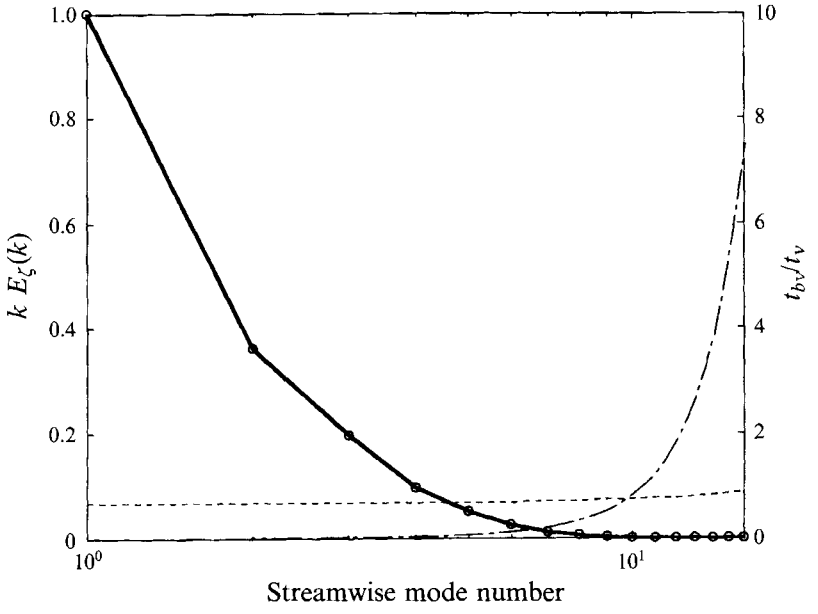

FIGURE 11. Ratio of buoyancy to viscous timescales as a function of streamwise mode number for spanwise and vertical mode numbers of 5 and 28 respectively. The ratio is plotted for the hyperviscosity used in these simulations (———) and for physical viscosity with $Re = 100$ (----). The displacement power spectrum, corresponding to figure 8 at $t = 21$, is also shown (-o-o-o-). Nearly all the energy of the wave instability resides in spatial modes where $t_v \gg t_{bv}$.

buoyancy timescale at the observed spatial scales of the wave instability. A much higher-resolution numerical model would be required to allow sufficiently large Reynolds numbers to simulate the instability directly without excessive damping. This is precisely why large-eddy rather than direct simulations were conducted.

5. Energetics of waves at critical levels

We now examine the energetics of the interaction of internal waves with a mean shear flow. An energy equation, describing the balance within a fixed volume V, is used to quantify the energy flow associated with internal waves approaching a critical level. The volume of interest encloses the critical level as well as that region of the domain in which the waves are observed to become unstable. The volume V is bounded above and below by horizontal planes S_1 and S_2 located at $z = 7$ and $z = 5$ respectively. Initially, the energy in V is approximately zero. Energy is input to V in the form of downward-propagating waves. Through interaction with the ambient shear, a number of processes occur, including mean flow acceleration, wave reflection, diffusive mixing and dissipation. Our objective is to quantify the distribution of the incident energy between these processes.

The kinetic and potential energies, E_k and E_p respectively, are defined as integrals over V,

$$E_k = \frac{1}{2}\int_V (u^2+v^2+w^2)\,\mathrm{d}V, \tag{11}$$

$$E_p = Ri\int_V \rho(z-z_{ref})\,\mathrm{d}V, \tag{12}$$

where z_{ref} is an arbitrary reference height. The total energy E_{tot} is then the sum of the

kinetic and potential energies. Evolution equations for E_k and E_p can be derived from the equations of motion (1)–(3):

$$\frac{\mathrm{d}}{\mathrm{d}t}E_k = -\oint_S w[p+\tfrac{1}{2}(u^2+v^2+w^2)]\,\mathrm{d}S - Ri\int_V \rho w\,\mathrm{d}V + \int_V \boldsymbol{u}\cdot\mathscr{D}(\boldsymbol{u})\,\mathrm{d}V, \tag{13}$$

$$\frac{\mathrm{d}}{\mathrm{d}t}E_p = -Ri\oint_S \rho w(z-z_{ref})\,\mathrm{d}S + Ri\int_V \rho w\,\mathrm{d}V + \int_V (z-z_{ref})\mathscr{D}(\rho)\,\mathrm{d}V. \tag{14}$$

Adding these two equations yields the balance equation for the total energy in V:

$$\frac{\mathrm{d}}{\mathrm{d}t}E_{tot} = -\oint_S w[p+\tfrac{1}{2}(u^2+v^2+w^2)]\,\mathrm{d}S - Ri\oint_S \rho w(z-z_{ref})\,\mathrm{d}S + \int_V [\boldsymbol{u}\cdot\mathscr{D}(\boldsymbol{u}) + (z-z_{ref})\mathscr{D}(\rho)]\,\mathrm{d}V. \tag{15}$$

5.1. *Sources and sinks*

Since periodic boundary conditions are imposed in the $\hat{x}$- and $\hat{y}$-directions, the surface integrals need only be evaluated on S_1 and S_2. The first term on the right-hand side of (15) is the rate of kinetic energy flux, while the second term is the rate of potential energy flux. For ideal waves, i.e. unbounded linear internal waves, the first term is non-zero while the second term vanishes because ρ' and w are out of phase. Contributions resulting from this second term, then, are second-order wave effects. Owing to the trapping effect of the critical level, the isopycnal displacements are very small near S_2 compared to those near S_1. If we now prescribe the reference level z_{ref} to correspond with S_1, the flux rate for potential energy vanishes on S_1. Thus, (15) states that the total energy in V can change as a result of kinetic energy flux across the upper and lower surfaces, through molecular dissipation, or, to a much smaller extent, through net mass flux across S_2. We will use this balance equation to quantify the energy flow in the system.

The sources and sinks of energy can be evaluated directly from (15), simply integrating the flow field in space to get the rates, and integrating in time to get the cumulative gains and losses. Note however that, if we integrate the flux rate through S_1, we are measuring the net energy flux E_{net}, resulting from both incident and reflected waves. To separate the two, we also carried out free wave calculations in which no ambient shear flow is prescribed. In the absence of any interaction, these waves simply flux energy into V through S_1 and out again through S_2. We define the incident energy E_{in} to be the energy fluxed in through S_1 in the free wave calculations. The wave energy reflected E_{refl} is then the difference between E_{net} and E_{in}.

5.1.1. *Sources*

The cumulative energy fluxes through the bounding planes S_1 and S_2 are shown in figure 12 for the linear, as well as the two- and three-dimensional nonlinear calculations. Early in the calculations, before about $t = 10$, only the leading edges of the wave packets have propagated across S_1 and so E_{in} increased only slowly. Most of the increase in E_{in} occurs between $t = 10$ and 35, as the most energetic portion of the packets arrives. The slight variability of E_{in} in (*b*) and (*c*) after about $t = 30$ indicates an enhancement of dispersion, or the tendency for wave components to separate, through nonlinear effects.

The energy reflected is indicated by the shaded regions. Reflection becomes significant after about $t = 25$ and $t = 30$ in the nonlinear calculation and linear calculations

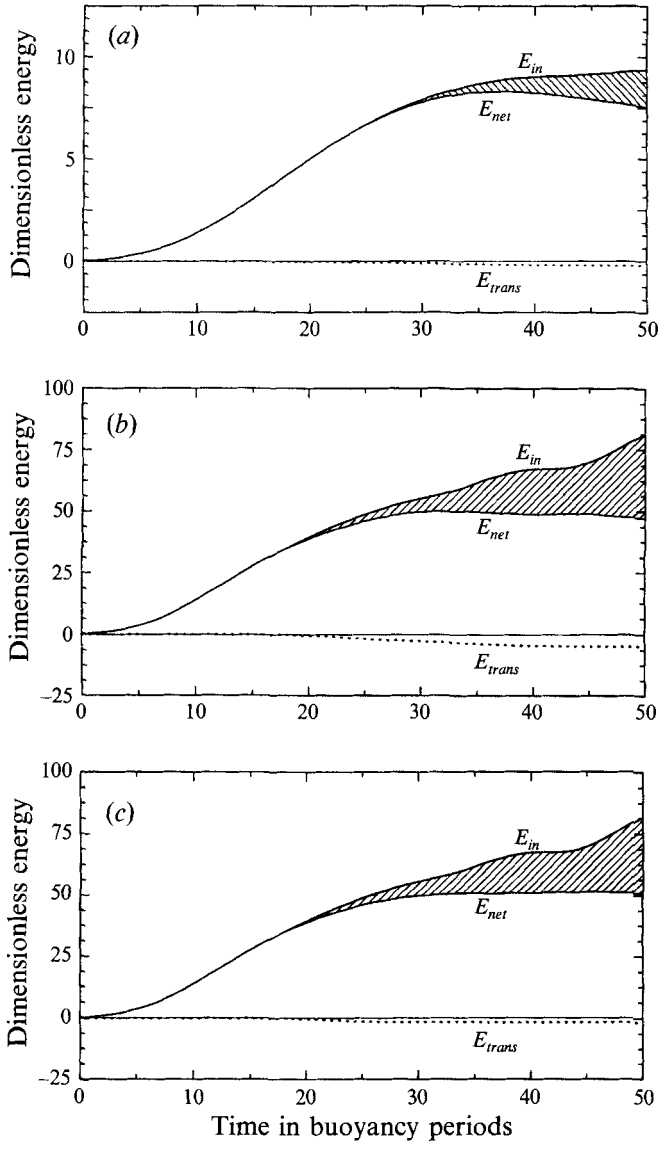

FIGURE 12. Incident energy E_{in}, net energy fluxes E_{net}, and E_{trans} through upper and lower bounding surfaces. Results are shown for the (*a*) three-dimensional linear, (*b*) two-dimensional nonlinear and (*c*) three-dimensional nonlinear calculations.

respectively. Relative to E_{in}, nonlinearity enhances reflection approximately twofold. After about $t = 30$, the net energy flux through S_1 begins to decrease slightly in the linear case, indicating more upward- than downward-propagating energy late in the calculation. During the corresponding time period in the nonlinear cases, the net rate of energy flux is approximately zero, as a balance is maintained between incidence and reflection.

The transmitted energy E_{trans} is found by integrating the transmission rates over the lower bounding surface S_2:

$$E_{trans} = \int_0^t \oint_{S_2} w[p+\tfrac{1}{2}(u^2+v^2+w^2)]\,\mathrm{d}S\,\mathrm{d}\tau + Ri\int_0^t \oint_{S_2} \rho w(z-z_{ref})\,\mathrm{d}S\,\mathrm{d}\tau. \qquad (16)$$

In all cases the transmitted energy E_{trans} is less than zero. By the sign convention of (16), negative values indicate a net flux of energy *into* V through S_2. In the three-dimensional nonlinear case, this flux occurs primarily between about $t = 22$ and 25, during the period that overturns are present near the critical level. The flux is maintained for a much longer period of time, again correlated with the overturning features, in the two-dimensional calculation.

5.1.2. *Sinks*

The energy losses due to viscous and diffusive effects, D_k and D_p respectively, are also evaluated by direct integration:

$$D_k(t) = \int_0^t \int_V \boldsymbol{u} \cdot \mathscr{D}(\boldsymbol{u}) \, \mathrm{d}V \, \mathrm{d}\tau, \tag{17}$$

$$D_p(t) = \int_0^t \int_V (z - z_{ref}) \mathscr{D}(\rho) \, \mathrm{d}V \, \mathrm{d}\tau. \tag{18}$$

Figure 13 shows the cumulative losses D_k and D_p.

For all three calculations $|D_p| \ll |D_k|$, although substantially less so in the linear case. In each of these cases, the dissipation rates of both kinetic and potential energy are low until about $t = 20$, when the isopycnal displacements are largest. In the three-dimensional nonlinear calculation, approximately 95% of the kinetic energy dissipation occurs after $t = 20$, when the convective cells are clearly visible in figure 6. The dissipation rates of kinetic energy remain nearly constant after about $t = 22$, implying a nearly uniform rate of energy flux to small scales. It is noteworthy that the total amount of kinetic energy dissipated in the three-dimensional case is nearly twice that in two dimensions. In the two-dimensional case, the energy transfer to small scales is essentially laminar, caused by the continued refraction of the steep waves near the critical level by the ambient shear. The cascade of energy in the three-dimensional case is controlled by the dynamics of wave instability rather than wave/mean flow interaction. Apparently, the transition of the flow from two to three dimensions through convective instability enhances the cascade of energy to small scales.

It is also interesting to compare the energy losses between the linear and nonlinear calculations. If the dynamics were strictly linear, the amount of kinetic energy loss in the large-amplitude simulations would simply be nine times the energy loss of the small-amplitude case. In fact, the loss of kinetic energy in the two-dimensional case is only about 76% of this value while in the three-dimensional case it is 121%. Despite the twofold increase in reflection, the total amount of kinetic energy driven to the dissipation scales increases substantially in the three-dimensional case. These results imply that the dynamics of fluid instabilities at moderate scales may largely determine the energetics of the resulting small-scale turbulence.

5.2. *Energy partition*

The total energy within V can also be partitioned into various categories. Loosely speaking, we split both the kinetic and potential energies into mean and perturbation components. The utility of any such splitting depends on the degree to which the averaging operations isolate different physical processes. For kinetic energy, it seems natural to define mean velocities with respect to horizontal averaging over an integer number of wavelengths, since we are interested in quantifying the acceleration of the horizontally averaged mean flow. Horizontal averaging is not a good choice for the

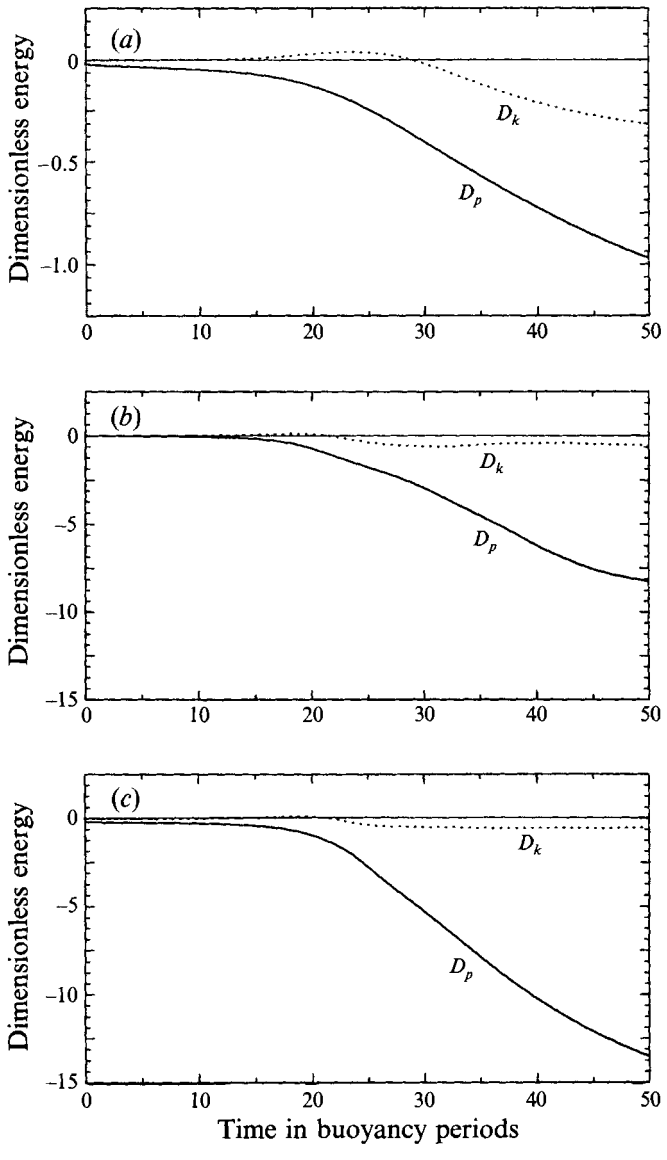

FIGURE 13. Cumulative losses of kinetic and potential energy for (*a*) three-dimensional linear, (*b*) two-dimensional nonlinear and (*c*) three-dimensional nonlinear calculations.

density field, however, if the interest is in quantifying the diffusive mixing of the fluid. For the problem considered here, the potential energy of the horizontally averaged density is influenced substantially more by adiabatic buoyancy flux than by diffusive mixing (Winters & D'Asaro 1991, 1994). To quantify mixing, it is better to split the potential energy between available and background components. The available potential energy is the amount of energy released if the fluid were to adiabatically attain a configuration of minimum potential energy. The background potential energy is simply that of the minimum energy configuration. Aside from changes in potential energy due to net mass flux into V, which can be calculated and corrected for, the background potential energy can only change as result of diffusive mixing. Conversely, changes in the background potential energy, corrected for net mass flux, represent

energy expended in mixing the fluid. The available potential energy is energy still available to be converted to other forms, i.e. to kinetic or background potential energy. Regarding the transfer of energy to the mean states as sinks, we can think of the sum of the available potential and perturbation kinetic energies as the energy of the flow that is, in some sense, still active. A more complete discussion of the potential energy budget is given in Winters & D'Asaro (1991, 1994).

Thus, the kinetic energy is split between mean and fluctuating components with respect to horizontal averaging. The potential energy is decomposed into available and background components, and corrected to eliminate the contribution due to net mass flux into V. Because the flow contains relatively large amounts of mean kinetic and background potential energy initially, only changes in these mean states are of interest. We define

$$(E_k)_M(t) = \Delta \frac{1}{2} \int_5^7 \bar{u}^2 \, \mathrm{d}z, \tag{19}$$

$$E_{mix}(t) = \Delta Ri \int_V \rho z_* \, \mathrm{d}V + \int_0^t Ri \oint_{S_2} \rho w (z - z_{ref}) \, \mathrm{d}S \, \mathrm{d}\tau \tag{20}$$

to be the relevant changes in mean kinetic and background potential energy. Here Δ indicates a change with respect to the initial value and an overbar signifies spatial averaging. The vertical location of a fluid parcel in the minimum-energy configuration is denoted by z_*. Numerically, the correction associated with mass flux through S_2 turns out to be relatively small. The perturbation kinetic energy and available potential energy are

$$(E_k)_P(t) = E_k - (E_k)_M(t), \tag{21}$$

$$E_a(t) = Ri \int_V \rho (z - z_*) \, \mathrm{d}V. \tag{22}$$

Figure 14 shows the distribution of energy within V as a function of time. Early in the calculations, before about $t = 10$, only E_a and $(E_k)_P$ are increasing as the wave packets enter V but have not yet reached the vicinity of the critical level. The two curves are almost coincident during this time, indicating approximate equipartition of wave energy. Later, an exchange of energy is apparent as E_a and $(E_k)_P$ oscillate in time. This exchange is a second-order wave effect which occurs even in the small-amplitude calculation. The oscillations cease at about $t = 30$. While there is a slight bias toward excess potential energy in the two-dimensional case, and excess kinetic energy in the linear case, both calculations exhibit approximate equipartition by $t = 50$. In the three-dimensional nonlinear case, however, a significant bias towards excess kinetic energy emerges shortly after $t = 20$, which corresponds to the time period when the vortical mode becomes energized. The excess perturbation kinetic energy is approximately equal in magnitude to the horizontal kinetic energy of the vortical mode at the end of the calculation. We interpret this as the result of energy transfer to the potential vorticity carrying quasi-horizontal motions.

Beginning about $t = 10$, $(E_k)_M$ starts to increase as the waves near the critical level accelerate the mean flow. Mean flow acceleration continues at a nearly uniform rate until about $t = 40$, for both the two-dimensional and the linear calculations, but drops off considerably at about $t = 30$ in the three-dimensional case. Again, we can compare the total amount of mean flow acceleration for the large-amplitude cases to that obtained by scaling up the small-amplitude case. In contrast to D_k, however, nonlinear values of $(E_k)_M$ are much less than the scaled linear value; only about 69% and 60% for the two- and three-dimensional cases respectively. Apparently, the increased

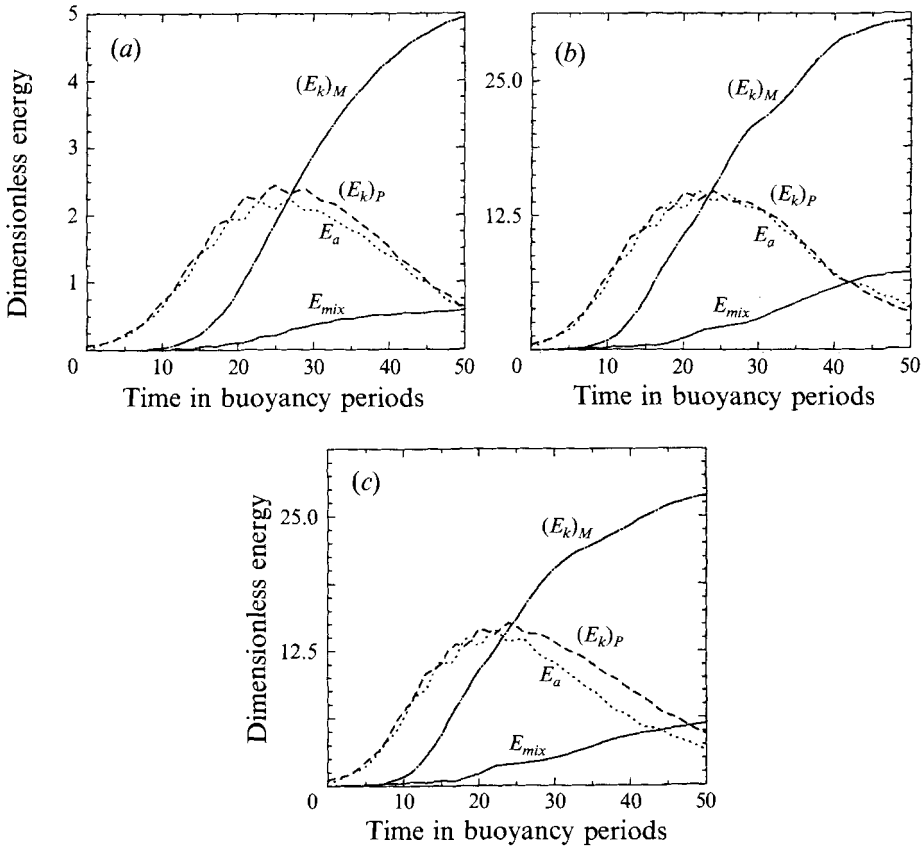

FIGURE 14. Energy partition within V. Kinetic energy is split between horizontal mean and perturbation components $(E_k)_M$ and $(E_k)_P$. Potential energy is decomposed into available and background (corrected for net mass flux) potential energies E_a and E_{mix}. (*a*) Three-dimensional linear, (*b*) two-dimensional nonlinear, (*c*) three-dimensional nonlinear calculations.

reflection and kinetic energy dissipation occur primarily at the expense of mean flow acceleration.

The energy expended in mixing the stratification, E_{mix}, only begins to increase significantly after about $t = 18$. This corresponds to the time period of maximum isopycnal displacements. A relatively uniform rate of increase in E_{mix} is maintained throughout the calculations. In all cases, significantly less energy is transferred to background potential than to mean kinetic energy. Relatively more mixing occurs in both the large-amplitude calculations than in the small-amplitude case. The final values of E_{mix} are 135% and 109% of the scaled linear result.

The largest energy transfer in the wave critical-level interaction is to the ambient shear flow. An important issue is whether mean flow acceleration, coupled with weakening of the stratification through mixing, tends to stabilize or destabilize the ambient flow. Figure 15 shows the evolution of the mean flow profiles and the minimum values of the gradient Richardson number. Though the mean flow accelerates, the mean shear decreases. This effect is partially offset by diffusive mixing and the net result is an overall increase in the gradient Richardson number and hence the stability of the flow. This result is likely to be sensitive to the ratio of characteristic lengthscales of the mean shear flow and the incident wave.

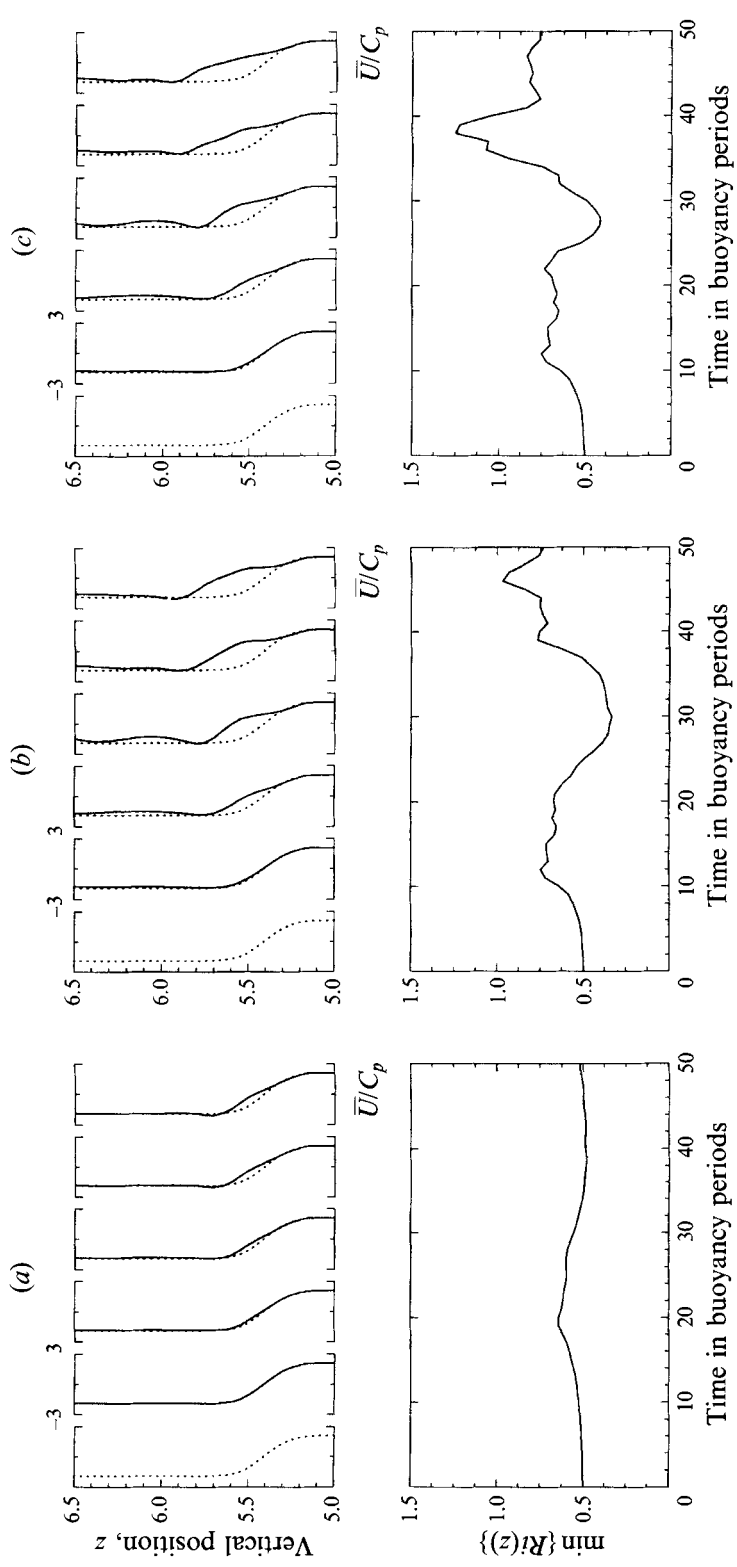

FIGURE 15. Horizontally averaged velocity profiles at several points in time. Also shown is the minimum gradient Richardson number as a function of time. Despite the acceleration of the mean flow near the critical level, the gradient Richardson number, and hence the stability of the mean flow, increase with time. (*a*) Three-dimensional linear, (*b*) two-dimensional nonlinear and (*c*) three-dimensional nonlinear calculations.

	2D nonlinear	3D nonlinear	Scaled linear	3D linear
E_{in}	81.25 (94.4%)	81.25 (97.9%)	84.25 (97.8%)	9.36
E_{trans}	−4.75 (5.6%)	−1.75 (2.1%)	−2.00 (2.2%)	−0.22
E_{refl}	34.00 (39.5%)	30.25 (36.5%)	16.25 (18.9%)	1.81
E_{loss}	8.75 (10.2%)	14.00 (16.9%)	11.50 (13.5%)	1.28
$(E_k)_M$	30.50 (35.6%)	27.00 (32.5%)	44.50 (51.7%)	4.94
$(E_k)_P$	3.50 (4.0%)	4.75 (5.7%)	5.25 (6.1%)	0.58
E_a	3.75 (4.3%)	3.25 (3.8%)	5.75 (6.6%)	0.64
E_{mix}	7.00 (8.2%)	5.75 (6.9%)	5.25 (6.1%)	0.58
Total in V	86.00 (100%)	82.75 (100%)	86.00 (100%)	9.56
Accounted for	87.50 (101.9%)	84.75 (102.4%)	88.50 (102.8%)	9.83

TABLE 1. Dimensionless energy partition

The energy balance presented in this section allows the effects of nonlinearity and three-dimensionality to be examined independently and quantitatively. A summary of the energy partition between flow components at the end of the calculations is given in table 1. Three calculations are summarized in table 1. The top headings indicate the initial conditions for each simulation. Again, the terms linear and nonlinear indicate only the initial amplitude of the incident wave packet; the equations solved were fully nonlinear in all cases. As indicated in §3, the calculations labelled 3D were initialized with a small-amplitude three-dimensional noise field as well as the two-dimensional wave packet and ambient shear flow. The flow in these cases is then free to evolve in three dimensions. The designation 2D indicates that no noise field was initialized and hence the evolution remains strictly two-dimensional. To facilitate comparison with the nonlinear results, the results of the linear case have also been scaled up to the energy level of the nonlinear calculations. The labels to the left indicate specific categories of energy, each having been defined previously.

The dimensionless energy values are given for each category. These values are then converted to percentage of the total energy input to V. Note that most of the energy input was fluxed in through the upper boundary S_1 and thus appears in E_{in}. These values are not 100% however, because a small amount of energy flux into V occurred across the lower surface S_2. This energy appears as negative values of E_{trans}. The bottom two rows give an indication of the total error in the calculations. The 'Total in V' figures are simply the sums of the energy fluxes into the region of interest. The 'Accounted for' values are then the sums of the estimates of each category. Ideally, these two should agree. Our results agree only to within about 3%.

For the linear critical-level interaction, approximately 50% of the wave energy is expended in accelerating the mean flow, nearly 20% is reflected, and about 13% is still in the form of internal waves at the end of the calculation. The remaining wave energy is driven to small scales with about 6% mixing the ambient stratification and about 14% appearing in E_{loss}, i.e. viscously or diffusively dissipated.

The energy distribution is sensitive to the incident wave amplitude, as can be seen by comparing the scaled linear results with either of the nonlinear cases. The relative amount of mean flow acceleration decreases substantially, with only about 36% and 33% of the wave energy converted to $(E_k)_M$ in the two- and three-dimensional cases respectively. The relative amount of reflection, however, is enhanced by a factor of about two.

Three-dimensional effects are also evident. Three-dimensionality enhances the

cascade of energy to small scales, increasing the dissipation of energy by a factor of about 1.7 in comparison to the two-dimensional case. It is interesting to note that, despite the substantial increase in total dissipation, the total mixing of the ambient stratification actually decreases slightly. Further, the excess $(E_k)_P$ in comparison to E_a is related to the excitation of vortical modes.

6. Discussion

A series of calculations was performed in an effort to study the dynamics and energetics of internal wave breakdown at critical levels. Both large- and small-amplitude wave packets were allowed to propagate into a shear flow toward a critical level. Large-amplitude internal waves were observed to break down at critical levels through an instability process. The effects of both shear and buoyancy contribute to the instability mechanism and the interaction between these two effects results in the intrinsically three-dimensional nature of the instability. Ultimately the instability is convective: overturned isopycnals lead to counter-rotating vortices similar to convective cells. The orientation and energetics of these vortices, however, are strongly influenced by the intensified wave shear. The wave packets simulated here break down neither by a simple advective instability nor by a simple shear instability but by a three-dimensional instability with elements of both. One conclusion to be drawn from this result is that when both convection and shear are important, three-dimensional dynamics may be important. Constraining a model to only two dimensions may have unexpected consequences.

The simulation of wave instability provides a detailed view of a single event which results in the formation of nearly horizontal motions containing vertical vorticity. This aspect is of particular interest as neither the ambient shear flow nor the incident wave packet carry any potential vorticity. It should be noted that this form of instability occurred only in the presence of a three-dimensional noise field. In the absence of noise, the flow remains two-dimensional and no potential vorticity is generated.

The energetics of the interaction were also investigated. A detailed energy budget was used to quantify the distribution of energy between various flow components. The two most important processes energetically were wave reflection and mean flow acceleration. For the large-amplitude incident waves, and a gradient Richardson number of $\frac{1}{2}$ at the criticallevel, 35–40% of the wave energy was reflected. These percentages are close to the 35% reflectivity reported by Breeding (1971) for an ambient Richardson number of 0.53, though one should be wary of a direct comparison as the reflectivity depends on wave amplitude as well as other factors. About 35% of the incident wave energy was expended in accelerating the mean flow for the large-amplitude cases. Mean flow acceleration is apparently sensitive to wave amplitude as the percentage increased to slightly over 50% for the small-amplitude case. In either case, the observed mean flow acceleration is much less than the 82% observed by Thorpe (1987).

Because of the large fractions of energy reflected and absorbed, only a relatively small amount is available to mix the ambient stratification. In fact, only about 20–25% of the incident energy ends up driven to small scales where is it subjected to diffusive and viscous effects. Only a fraction of this energy goes to mixing. A more detailed analysis of the small-scale mixing and dissipation and associated with this event is discussed in Winters & D'Asaro (1991, 1994).

The authors gratefully acknowledge the support of this work by the National Science Foundation, Grant Nos. OCE-9000166 and OCE-9302143. We also appreciate the many discussions with James Riley, Terry Ewart, Steve Reynolds and Harvey Seim.

REFERENCES

BREEDING R. J. 1971 A nonlinear investigation of critical levels for internal atmospheric gravity waves. *J. Fluid Mech.* **50**, 545–563.

BRETHERTON, F. P. 1966 The propagation of groups of internal gravity waves in a shear flow. *Q. J. R. Met. Soc.* **92**, 466–480.

DOMARADZKI, J. A., METCALFE, R. W., ROGALLO, R. S. & RILEY, J. J. 1987 Analysis of subgrid eddy viscosity with use of results from direct numerical simulations. *Phys. Rev. Lett.* **58**, 547–550.

DRAZIN, P. G. & REID, W. H. 1981 *Hydrodynamic Stability*. Cambridge University Press.

FARGE, M. 1987 Dynamique non-lineaire des ondes et des tourbillons dans les equations de Saint-Venant. These de Doctorat d'Etat et Sciences Mathematique, Univesite Paris VI.

FRITTS, D. C. 1982 The transient critical level interaction in a Boussinesq fluid. *J. Atmos. Sci.* **87**, 7797–8016.

FRITTS, D. C. & GELLER, M. A. 1976 Viscous stabilization of gravity wave critical level flows. *J. Atmos. Sci.* **33**, 2276–2284.

HAZEL, P. 1967 The effect of viscosity and heat conduction on internal gravity waves at a critical level. *J. Fluid Mech.* **30**, 775–783.

HENYEY, F. S., WRIGHT, J. & FLATTE, S. 1984 Energy and action flow through the internal wavefield: an eikonal approach. *J. Geophys. Res.* **91**, 8487–8495.

KOOP, C. G. 1981 A preliminary investigation of the interaction of internal gravity waves with a steady-shearing motion. *J. Fluid Mech.* **113**, 347–386.

KOOP, C. G. & MCGEE, B. 1986 Measurements of internal gravity waves in a continuously stratified shear flow. *J. Fluid Mech.* **172**, 453–480.

LELONG, M. P. 1989 Weakly nonlinear internal wave/vortical mode interactions in stably-stratified flows. PhD thesis, University of Washington.

LIN, C. L., FERZIGER, K. H., KOSEFF, J. R. & MONISMITH, S. G. 1993 Simulation and stability of two dimensional internal gravity waves in a stratified shear flow. *Dyn. Atmos. Oceans* **19**, 325–366.

LIN, J. T. & PAO, Y. H. 1979 Wakes in stratified fluids. *Ann. Rev. Fluid Mech.* **11**, 317–338.

STAQUET, C. & RILEY, J. J. 1989*a* A numerical study of a stably-stratified mixing layer. In Selected Papers from the *Sixth Symposium on Turbulent Shear Flows, Springer, Berlin*, pp. 381–397.

STAQUET, C. & RILEY, J. J. 1989*b* On the velocity field associated with potential vorticity. *Dyn. Atmos. Oceans* **14**, 93–123.

THORPE, S. A. 1981 An experimental study of critical layers. *J. Fluid Mech.* **193**, 321–344.

THORPE, S. A. 1987 Transitional phenomena and the development of turbulence in stratified fluids: A review. *J. Geophys. Res.* **92**, 5231–5248.

WALTERSCHEID, R. L. & SCHUBERT, G. 1990 Nonlinear evolution of an upward propagating gravity wave: overturning, convection, transience and turbulence. *J. Atmos. Sci.* **49**, 101–125.

WHITHAM, G. B. 1974 *Linear and Nonlinear Waves*. Wiley.

WINTERS, K. B. & D'ASARO, E. A. 1989 Two dimensional instability of finite amplitude internal gravity wave packets near a critical level. *J. Geophys. Res.* **94**, 12709–12719.

WINTERS, K. B. & D'ASARO, E. A. 1991 Diagnosing diapycnal mixing. In *Proc. Hawaiian Winter Workshop: Dynamics of Oceanic Internal Gravity Waves, University of Hawaii at Manoa*, pp. 279–294.

WINTERS, K. B. & D'ASARO, E. A. 1994 Available potential energy and mixing in density-stratified fluids. *J. Fluid Mech.* (submitted).

WINTERS, K. B. & RILEY, J. J. 1992 Instability of internal waves near a critical level. *Dyn. Atmos. Oceans* **16**, 249–278.